Advanced Powder Technology 30 (2019) 1765–1781

Contents lists available at ScienceDirect

Advanced Powder Technology

journal homepage: www.elsevier.com/locate/apt

Original Research Paper

Continuous high-shear granulation: Mechanistic understanding of the influence of process parameters on critical quality attributes via elucidating the internal physical and chemical microstructure

Wei Meng [a], Jakub Dvořák [c], Ravish Kumar [b], Rudy Hofmeister [d], František Štěpánek [c], Rohit Ramachandran [b], Fernando J. Muzzio [a,b,*]

[a] Department of Pharmaceutics, Rutgers University, Piscataway, NJ 08854, USA
[b] Department of Chemical and Biochemical Engineering, Rutgers University, Piscataway, NJ 08854, USA
[c] Department of Chemical Engineering, University of Chemistry and Technology, Prague, Technická 3, 166 28 Praha 6, Czech Republic
[d] H2Optx, Inc, San Jose, CA 95119, USA

ARTICLE INFO

Article history:
Received 7 March 2019
Received in revised form 22 April 2019
Accepted 28 April 2019
Available online 8 June 2019

Keywords:
Continuous manufacturing
Wet granulation
Quality by design
Tablet dissolution
Microstructure
Drug agglomeration

ABSTRACT

Over the past decade, continuous wet granulation has been emerging as a promising technology in drug product development. In this paper, the continuous high-shear mixer granulator, Lödige CoriMix® CM5, was investigated using a low-dose formulation with acetaminophen as the model drug. Design of experiments was deployed in conjunction with multivariate data analysis to explore the granulator design space and comprehensively understand the interrelation between process parameters and critical attributes of granules and tablets. Moreover, several complementary imaging techniques were implemented to unveil the underlying mechanisms of physical and chemical microstructure in affecting the tablet performance. The results indicated that L/S ratio and impeller speed outweighed materials feeding rate in modifying the granule and tablet properties. Increasing the degree of liquid saturation and mechanical shear input in the granulation system principally produced granules of larger size, smaller porosity, improved flowability and enhanced sphericity, which after compression generated tablets with slower disintegration process and drug release kinetics due to highly consolidated physical microstructure. Besides, in comparison to batch mixing, continuous mixing integrated with a conical mill enabled better powder de-agglomeration effect, thus accelerating the drug dissolution with increased surface area.

1. Introduction

In recent years, due to the increasing demand for solid dosage forms and expiring patents of drug molecules, there is a critical need to accelerate and de-risk process and product development. In such a context, continuous manufacturing has been drawing considerable attention by virtue of its intrinsic advantages [1,2]. It enables the prospect of curtailing capital expenditure with smaller equipment footprint and elimination of intermediate storage, and facilitating process design and understanding with less scale-up issues. In addition, risk mitigation and enhanced product quality can be accrued with integration of process analytical technologies for automated real-time quality monitoring and control [3]. More importantly, regulatory authorities, such as the U.S. Food and Drug Administration (FDA) and European Medicines Agency (EMA), also encourage and incentivize pharmaceutical industry to adopt such a paradigm transformation from conventional batch processing to more futuristic and advantageous continuous processing [4].

Wet granulation has been one of the most prevalent unit operations in tablet manufacturing. It creates interparticle bonds and promotes granule growth with the induction of liquid binder and mechanical shear forces in the system [5]. By combining formulation design with process optimization, particle characteristics can be modified, which herein exerts an impact on the performance of finished product. Key primary properties of granules are size distribution and porosity that dominate a wide spectrum of secondary properties, such as flow properties, strength and compressibility [6]. Pharmaceutical quality by design (QbD) principles framed by ICH Q8, Q9 and Q10 guidelines underline that product and process

* Corresponding author at: 98 Brett Road, Department of Chemical and Biochemical Engineering, Rutgers University, Piscataway, NJ 08854, USA.
E-mail address: fjmuzzio@yahoo.com (F.J. Muzzio).

https://doi.org/10.1016/j.apt.2019.04.028
0921-8831/

understanding and control predicated on sound science and quality risk management are of essence to increase process capability and robustness, enhance efficiencies of product development and manufacturing, accomplish performance-based quality specifications etc. Those efforts are made to ensure consistent satisfaction of predefined quality target product profiles and eventually build rather than test quality into the end product [7,8].

To identify, monitor and control the critical sources of variability in continuous wet granulation processes, correlations between critical material attributes, critical process parameters and critical quality attributes have been extensively examined and reported in literature over the past few years [9–13]. Willecke et al. (2018) implemented a novel approach to explore the influence of overarching excipient characteristics on granule and tablet attributes by combining Design of Experiments (DoE) with principal component analysis [14]. With the aid of near-infrared chemical imaging, Kumar et al. (2016) investigated the residence time and liquid distributions under different combinations of process and equipment design parameters [15]. Screw speed was found to be the most dominant variable in enhancing axial mixing and granulation yield accompanied by reduced mean residence time. EI Hagrasy et al. (2013) delved into the fundamental granulation rate processes with different screw configurations in the kneading section. 90° neutral and 30° reverse offset angles of kneading elements featured the two extremes of granulation mechanisms: breakage followed by layering, and shear-elongation and breakage followed by layering, respectively [16].

While the intrinsic dissolution rates of active ingredient are determined by the chemical nature of the compound itself, tablet microstructure carrying information about the history of manufacturing process enables additional degrees of freedom to modulate the dosage form bioavailability [17]. It is an essential factor that is closely intertwined with the mechanical strength, friability, disintegration, and drug dissolution and release kinetics of the finished product. One of the microstructures that has been studied by other researchers focused on the intra-granular physical structure at microscopic scale and its influence on spatial distribution of solid particles and void space within the tablet after compaction [18–21]. Typically, the observed relationship is that an increase in granule porosity is associated with a reduction in granule strength but greater compatibility, subsequently leading to faster tablet disintegration and dissolution. However, high porosity may result in unacceptably friable tablet with low elastic modulus and tensile strength, which, in turn, causes sub-potency and poor product quality during processing and handling. Some other contributions shed light on the implication of formulation microstructure at a comparable length scale concerning the homogeneity of interactive mixture or distribution of agglomerates formed by cohesive hydrophobic drug particulates on blend dissolution [22–25]. In absence of proper dispersion or de-agglomeration processing prior to the dissolution testing, particles formed coherent masses and manifested significant slower dissolution rate on account of reduced surface area exposed to the dissolution medium. Therefore, a better understanding of the interplay between material properties and process conditions is of paramount importance to engineer the microstructure that is further conducive to diagnosing deficiencies, avoiding pitfalls and ensuring consistent quality in product development [26,27].

There has been very limited research heretofore carried out to implement QbD methodologies towards continuous wet granulation processes. Our previously published work systematically investigated a continuous high-shear granulation system, Lödige CoriMix® CM5, with the focus on bridging knowledge gap between critical process variables and granule properties [18]. This present study continued the investigation to further include final drug product in the parametric analysis with emphasis on understanding the role of microstructure in modulating the performance of immediate release tablets. DoE, multivariate data analysis and complementary imaging techniques were combined to (1) reveal the interplay between key process parameters, intermediate properties and final drug product attributes, (2) elucidate the underlying dissolution mechanisms accompanied by distinct tablet physical microstructures, and (3) gain in-depth insight into the influence of tablet drug agglomerate size distribution (chemical microstructure) on release kinetics.

2. Materials and methods

2.1. Materials

The low-dose formulation comprised 8% (w/w) semi-fine acetaminophen (APAP, Mallinckrodt Inc, Raleigh, NC), 44.75% (w/w) α-lactose monohydrate 200 M (Foremost Farms USA, Baraboo, WI, USA), 44.75% (w/w) microcrystalline cellulose (MCC, Avicel® PH101, FMC Biopolymer, Philadelphia, PA) and 2.5% (w/w) polyvinylpyrrolidone (PVP K29-32, Fisher Scientific, Pittsburgh, PA). The dry binder addition method was adopted, i.e., PVP was premixed with other ingredients as dry powders. Distilled water as granulation liquid was injected into the system in dripping mode through a peristaltic pump. Several crucial physical specifications of each formulation constituent were listed in Table 1.

2.2. Production of granules

2.2.1. Continuous mixing (CM) of raw materials

With respect to the 17-run face-centered cubic design (refer to Section 2.3), all the excipients were firstly premixed in a Glatt tumble tote blender (Model TAM 40, Glatt GmbH, Binzen, Germany) for 30 min at 25 rpm, and then transferred into a K-Tron loss-in-weight (LIW) feeder (KT 35, K-Tron Soder, Niederlenz, Switzerland). Another K-Tron LIW feeder (KT 20) operated at gravimetric mode was used for feeding APAP (see Fig. 1(a)). The drug and excipients were then mixed in a Glatt convective continuous mixer (Model GCG-70) under 260 rpm with a total powder feeding rate of 30 kg/h. A Quadro conical screen mill (Comil®, Model #197S, Quadro Engineering, Ontario, Canada) was integrated into the experimental set-up upstream of the continuous mixer to de-lump agglomerates from incoming powder stream, thereby enhancing the dispersive mixing behavior with higher magnitude of shear stresses. The mill equipped with a 800 μm round-holed screen was operated at 1420 rpm.

2.2.2. Batch mixing (BM) of raw materials

A separate experiment was designed to examine the effect of drug agglomerate size distribution on tablet dissolution performance. In this study, raw materials were premixed by two different approaches. The first method was continuous mixing (refer to Section 2.2.1) whereas the second method was batch mixing where all ingredients were subjected to the gravity-driven low-shear batch mixing in the Glatt tumble tote blender (see Fig. 1(b)). The premixed raw materials were then transferred into a K-Tron LIW feeder (KT 20) for continuous granulation processing (see Fig. 1(c)). The purpose was to modify or manipulate the drug agglomerate size distribution only by distinct mixing methods while keeping the variables of downstream unit operations constant, i.e., identical granulation, compression and dissolution conditions. Conceivably, if tablets demonstrated substantial difference in drug release profiles, the cause can be traced back to the powder mixing approaches, namely the discrepancy in drug agglomerate size in mixture [23].

Table 1
Key physical specifications of formulation ingredients and premix.

Component	D10 (μm)	D50 (μm)	D90 (μm)	Bulk Density (g/ml)	Tapped Density (g/ml)	Hausner Ratio
APAP	5.5	29.8	116.4	–	–	–
MCC	19.1	58.7	132.5	–	–	–
Lactose	13.7	78.4	159.5	–	–	–
Premix	14.3	69.8	140.3	0.476	0.629	1.32

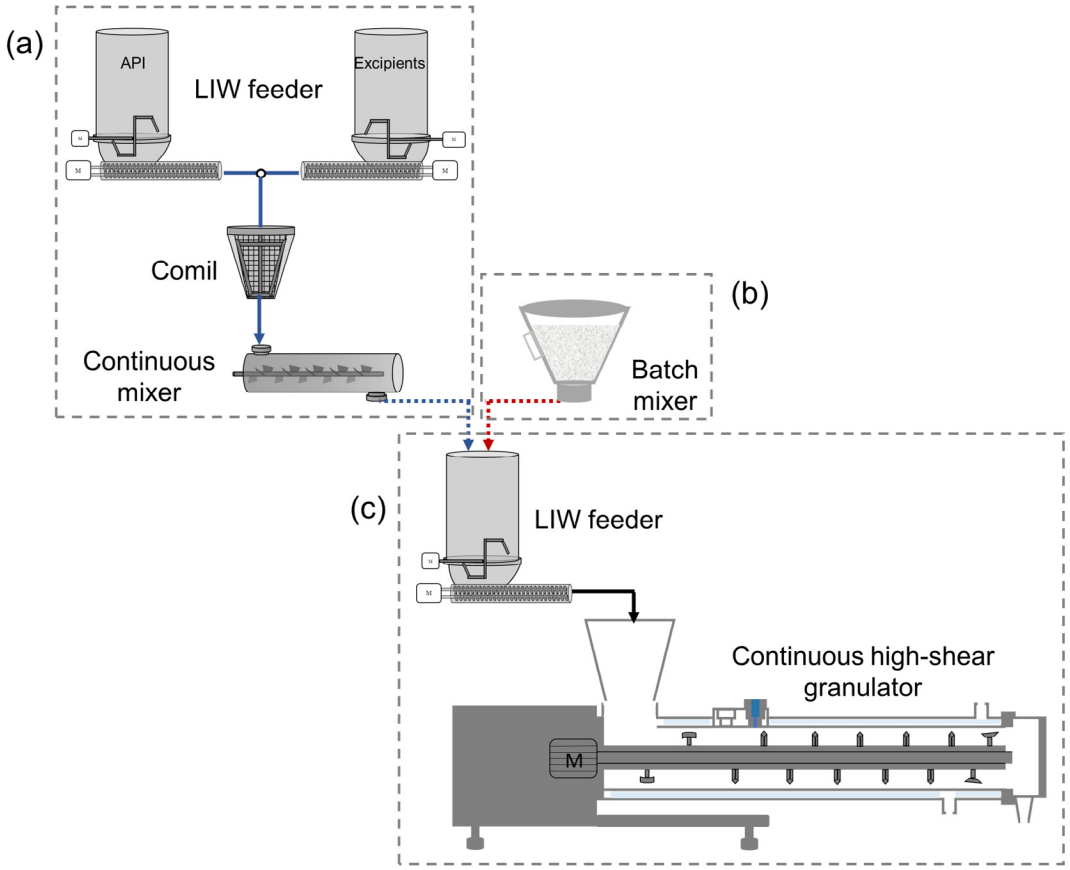

Fig. 1. Experimental set-up for granules production. (a) Continuous mixing of raw materials prior to granulation. (b) Batch mixing of raw materials prior to granulation. (c) Continuous high-shear granulation.

2.2.3. Continuous high-shear granulation

The premixed materials underwent continuous high-shear granulation in the Lödige CoriMix® CM5 granulator (Gebrüder Lödige Maschinenbau GmbH, Paderborn, Germany). It featured a horizontal drum inside which several plough-shaped blades or mixing pins were mounted along the rotary shaft to enable different functionalities: speeding up, granulation, and shaping of granules (Fig. 1(c)). The high rotation speed and concomitant large centrifugal force dominated the bulk flow over gravity, which formed a concentric annular layer of materials on the vessel wall moving through the chamber in a plug-like flow with the retention time dictated by processing parameters. The liquid components were introduced tangentially from the top into the product layer through a single phase nozzle in dripping mode, thereby ensuring a homogeneous distribution within the mixture and desisting from wetting the mixing wall and shaft.

2.3. Granulation experimental design and multivariate data analysis

In the current study, a face-centered cubic design augmented with three center points was employed to investigate the influence of three critical process parameters (CPPs, X-variables): rotation speed (x_1), L/S ratio (x_2) and throughput (x_3), on critical quality attributes (CQAs, Y-variables). Table 2 specified the levels of each investigated parameter as well as the characterized properties involved in the DoE. A total of 17 randomized experiments (see Table 3) were generated by JMP® statistical software (SAS Institute Inc., Cary, NC). Note that any "run #" mentioned in the following sections referred to the experiment RunOrder number in Table 3. In addition, the inverse calibration method of Projection to Latent Structures (PLS) regression was utilized to construct a PLS2 model with the SIMCA 14.1 software (Umetrics AB, Umeå, Sweden). Granule properties, tablet characteristics and the first moment of residence time distribution, mean residence time, were incorporated in the model as Y variables to delve into the interrelation between processing conditions, material flow profiles, and intermediates and finished drug product attributes.

2.4. Tablet compression

Granules from each experiment were air-dried at ambient conditions until the loss-on-drying moisture content was less than 3%.

Table 2
Independent variables and responses in the face-centered cubic design.

Predictor variables	Level			Response variables	
	Low	Intermediate	High	Granules	Tablets
Rotation speed (rpm)	1000	2000	3000	Granules size distribution; Shape; Porosity;	Tensile strength; Porosity; Friability;
L/S ratio	0.35	0.45	0.55	Bulk density; Tapped density; Flowability; Strength	Disintegration time; *in vitro* dissolution
Throughput (kg/h)	10	15	20		

Table 3
The 17-run face-centered cubic design for wet granulation.

RunOrder	Pattern	Rotation speed (rpm)	Throughput (kg/h)	L/S Ratio
1	000	2000	15	0.45
2	00A	2000	15	0.55
3	0a0	2000	10	0.45
4	0A0	2000	20	0.45
5	000	2000	15	0.45
6	a00	1000	15	0.45
7	000	2000	15	0.45
8	+ + –	3000	20	0.35
9	– – –	1000	10	0.35
10	+ – +	3000	10	0.55
11	– – +	1000	10	0.55
12	+ – –	3000	10	0.35
13	– + –	1000	20	0.35
14	00a	2000	15	0.35
15	– + +	1000	20	0.55
16	A00	3000	15	0.45
17	+ + +	3000	20	0.55

The dried granules were then sieved and the fractions between 250 and 710 μm were compacted into tablets by a tablet press emulator (Presster™, Metropolitan Computing Corporation, East Hanover, NJ) with an upper compaction force of 10 and 24 kN. It emulated the Fette Compacting 1200i tablet press (24 station). A round flat-faced punch was used to obtain cylindrical tablets with 10 mm diameter. Powder dosing weight was controlled around 350 mg for each tablet.

2.5. Granule characterization

2.5.1. Size distribution

Size distribution of granules was classified by sieve analysis utilizing a $\sqrt{2}$ series of sieves with mesh opening size ranging from 38 μm to 4 mm. The size distribution metrics (D10, D50, D90 and span) were then calculated based on the plot of normalized mass frequency (f_{mi}) shown in Eq. (1) versus the midpoint of each size interval on logarithmic scale [28].

$$f_{mi}(\ln x) = \frac{m_i}{\ln(\bar{n}_i / \bar{n}_{i-1})} \tag{1}$$

where m_i and $\bar{n}_i$ are the mass fraction and midpoint of size interval i, respectively.

2.5.2. Porosity

Granules in the size interval of 1.0–1.4 mm were collected and placed in a desiccator overnight prior to the measurement of true density (ρ_t) and envelope density (ρ_e) in the AccuPyc II 1340 helium pycnometer (Micromeritics, Norcross, GA) and Geopyc 1360 (Micromeritics, Norcross, GA), respectively. The granule porosity (ε_g) was then calculated by Eq. (2):

$$\varepsilon_g = 1 - \frac{\rho_e}{\rho_t} \tag{2}$$

2.5.3. Bulk and tapped densities

The bulk densities of granules (ρ_B) and premixed raw materials were determined by FT4 powder rheometer (Freeman Technology, Wayne, PA). Tapped densities (ρ_T) were tested via an automated tapped density analyzer (Quantachrome Instruments, Boynton Beach, FL) associated with a 250 ml graduated cylinder. Hausner ratio (HR) defined in Eq. (3) was used to characterize the granules flowability.

$$\mathrm{HR} = \frac{\rho_\mathrm{T}}{\rho_\mathrm{B}} \tag{3}$$

2.5.4. Strength

Granules in the size class of 250–710 μm were selected for the strength evaluation through a uniaxial confined compression test in Gamlen tablet press GTP-1 (Gamlen Tableting Ltd, Nottinghamshire, UK). 100 mg dried granules were compressed at a low strain rate of 5 mm/min with the 6 mm diameter die and punch set to a maximum applied load (P) of 250 kg. The fracture strength (τ) was then obtained by Eq. (4) [29],

$$\ln P = \ln\left(\frac{\tau}{\alpha}\right) + \alpha\varepsilon_n + \ln(1 - e^{-\alpha\varepsilon_n}) \tag{4}$$

where α stands for a constant related to Mohr-Coulomb failure criterion and ε_n represents the natural strain. τ and α were calculated by fitting Eq. (4) to plot natural logarithms of the applied load versus natural strain.

2.5.5. Particle shape

Eyecon™ three-dimensional (3D) particle characterizer (Innopharma Laboratories, Dublin, Ireland) operated in benchtop mode was employed to assess the shape of granules. The camera illumination is based on the principle of photometric stereo imaging, which detects the boundaries of overlapping particles and captures their 3D information. A set of best fitting ellipses can be derived with image gradient data that further determines the maximum ($D_{\max}$) and minimum ($D_{\min}$) particle diameters. The average aspect ratio (AR) calculated by Eq. (5) indicates the granule sphericity.

$$AR = \frac{D_{\max}}{D_{\min}} \tag{5}$$

2.5.6. Residence time distribution

Residence time distribution (RTD) for each DoE run was tested with 40 mg nigrosin stain as a pulse of tracer that was directly added into the feedstream once system reached the steady state. Granule samples were subsequently collected every 2 s up to 60 s and dissolved in 10 ml distilled water. The Cary 60 UV–Vis spectrophotometer (Agilent Technologies, Santa Clara, CA) at the wavelength of 578 nm was used to quantify the dye concentration in samples at different time points. The RTD function, $E(t)$, and its first moment, mean residence time (MRT), were calculated by Eqs. (6) and (7) as follows.

$$E(t) = \frac{c(t)}{\int_0^\infty c(t)dt} \tag{6}$$

$$\mathrm{MRT} = \int_0^\infty tE(t)\,dt \tag{7}$$

where $c(t)dt$ is the dye concentration (g/l) between time t and Δt.

2.6. Tablet characterization

2.6.1. Tensile strength

Tablet thickness was measured by a digimatic digital caliper (Mitutoyo America, Aurora, IL) and radial fracture force was determined in a hardness tester (MultiTest 50, SOTAX, Westborough, MA). Tablet tensile strength was then calculated by the following equation [30],

$$\sigma_t = \frac{2F}{\pi dh} \tag{8}$$

where σ_t was the tablet tensile strength (MPa), F was tablet fracture force (N), d and h were the tablet diameter (mm) and thickness (mm), respectively.

2.6.2. Porosity

The apparent density ρ_o of tablet was calculated by weight and volume. True density ρ_t of a crystalline solid was measured by a helium pycnometer (AccuPyc II 1340, Micromeritics, Norcross, GA). The tablet porosity ε_t can be obtained with Eq. (9).

$$\varepsilon_t = 1 - \frac{\rho_o}{\rho_t} \tag{9}$$

2.6.3. Friability

The unit mass of tablets was around 350 mg which is less than 650 mg, so eighteen tablets approximately corresponding to 6.5 g from each run were used for tests. Tablets were carefully dedusted and weighed (w_1) prior to being placed in a dual drum friability tester (PTF 20E, Pharma Test, Hainburg, Germany). The drum rotated 100 revolutions with the speed of 25 rpm for 4 min. After testing, samples were accurately weighed (w_2) again following the removal of any accumulated dust on the surface. The friability (FR) was expressed as the percentage weight loss in Eq. (10).

$$\mathrm{FR} = \frac{w_1 - w_2}{w_1} \tag{10}$$

2.6.4. Disintegration time

Six tablets from each DoE condition were evaluated for the disintegration time (T_d) in the Agilent 100 Automated disintegration apparatus (Agilent Technologies, Santa Clara, CA). The temperature and volume of distilled water in each beaker were 37.3 °C and 1000 ml, respectively. The end of each test was determined visually when no residue of the tablet was left on the basket mesh wire.

2.6.5. In vitro dissolution

Six tablets from each selected batch were dissolved in 900 ml phosphate buffer solution at pH 5.8 and 37.3 °C (USP ⟨7 1 1⟩). The dissolution apparatus (708-DS, Agilent Technologies, Santa Clara, CA) coupled with a UV/Vis spectrophotometer were utilized to measure acetaminophen absorbance at the wavelength of 248 nm every 3 min. The rotation speed of paddle was 50 RPM. Drug concentration at each time point was then derived from a standard UV calibration curve with the linear correlation (R^2 = 0.9996) from 4.9 * 10^{-5} to 0.05 g/L.

Parameters of assay time $t_{3\ \mathrm{min}}$, dissolution time $t_{90\%}$ and dissolution efficiency ($DE_{10\ \mathrm{min}}$) were used to characterize and compare the drug release profiles. $t_{3\ \mathrm{min}}$ and $t_{90\%}$ correspond to the percentage of drug dissolved after 3 min and the time necessary to release 90% of the drug, respectively. $DE_{10\ \mathrm{min}}$ defined in Eq. (11) is the area under the dissolution curve up to 10 min dissolution as a percentage of the area of the rectangle described 100% dissolution at the same time [31].

$$\mathrm{DE}_{10\ \mathrm{min}}\ (\%) = \frac{\int_0^t k \cdot dt}{k_{100} \cdot t} \cdot 100 \tag{11}$$

where k is the drug percent dissolved at time t.

2.6.6. Content uniformity

To evaluate the consistency of dosage units, 10 tablets were randomly selected from each batch and dissolved individually in a glass vial with 10 ml pure methanol before being placed in an incubator shaker (New Brunswick™ Excella® E25/E25R, Eppendorf, Hamburg, Germany) at 37.3 °C for 24 h. 5 ml samples were then withdrawn from the supernatant and diluted to the concentration range of calibration model from 0.0008 to 0.0128 g/L (R^2 = 0.9999). Same UV/Vis spectrophotometer was used to assay the drug content in each tablet based on its absorbance at 248 nm. An acceptance value (AV) was computed in Eq. (12) and compared to the passing criteria depicted in USP ⟨9 0 5⟩ uniformity of dosage units.

$$\mathrm{AV} = \left|M - \overline{X}\right| + k \times s \tag{12}$$

where $\overline{X}$ depicted the mean of individual contents, expressed as a percentage of the label claim (350 mg, 8% API in this case); k was the acceptability constant that equals to 2.4 when sample size is 10; s represented the sample standard deviation; M referred to the reference value (98.5% or 101.5%). The maximum allowed AV for sample size of 10 was 15.

2.7. Morphology and physical microstructure studies

2.7.1. Scanning electron microscopy (SEM)

The morphology of tablet surface was observed under the SIGMA Series of Field Emission Scanning Electron Microscopes (FE-SEM, Carl Zeiss Microscopy, Jena, Germany) operating at an accelerating voltage of 5 kV and high vacuum mode. Samples were stored in a vacuum desiccator overnight and then sputter-coated with 5 nm gold layer prior to tests.

2.7.2. X-ray micro-computed tomography (micro-CT)

Examination of the tablet internal structure was performed by Bruker microCT (SkyScan 1172, Billerica, MA). X-ray tomographic images were reconstructed to display the granules cross-sectional porous structure, and a 3D digital representation of individual granule was created to visually inspect the closed and open pores. The region of interest for each tablet selected in this study was a cycle on the surface with 4 mm in diameter. Shadow images with the pixel size of 4.89 μm were acquired with an optimized X-ray source at 40 kV (250μA) and scanned in the 0–180° interval using a 0.40° rotation step.

2.7.3. Magnetic resonance imaging (MRI)

MRI analysis enabled the observation of tablet disintegration process in 3D space. The elementary disintegration processes such as water ingress, leaching, erosion, break-up and potential structural changes could be revealed assisting in understanding the underlying disintegration mechanisms of tablet with distinct internal structures [32].

The Bruker MRI desktop system (ICON™, Billerica, MA) was used in conjunction with a custom-built flow cell where the tablet was placed. The analysis was on the basis of multi-slice multi-echo (MSME) sequence of pulses measuring the concentration of mobile hydrogen protons. The echo time was 20 ms and repetition time was 1200 ms. The image presented in this work was the middle slice and its resolution included a matrix size of 128 × 128 pixels

and field of view 1.8 × 1.8 cm. During testing, the flow cell was fixed by a holder with minimum contact area with tablet, thus preventing its movement in the dissolution medium.

2.7.4. Laser diffraction particle size distribution analysis

Following the disintegration time test, particle size of disintegrated tablets from different compression forces or granulation conditions were further measured by the laser diffraction analyzer (LA-950V2, HORIBA Scientific, Edison, NJ). The goal was to examine the integrity of granule internal structure after undergoing different tableting compression forces and illuminate the effect of physical microstructure on tablet disintegration and dissolution kinetics.

2.8. Drug agglomerate distribution and chemical microstructure studies

The 3D distribution of drug agglomerates in the tablets was investigated by a Raman imaging system (mPAT LAB-Pillerator, H2Optx, San Jose, CA). The device integrated Raman spectroscopy, microscopy, high-resolution optical imaging with automated X-Y-Z surface scanning. By interfacing the Pillerator sampling accessory with mPAT LAB, it enabled automatic sectioning of tablets with layer by layer hyperspectral imaging. After finishing the scan of multiple layers, a 3D chemical map and structural analysis of the tablet were established.

In the present study, the layer thickness was defined as 40 μm and in total 20 layers of each tablet was scanned. The field of view was 4 × 4 mm. The image scan settings were 50 Z steps with 2 μm for each step. The Raman scan settings included a XY resolution of 10 × 10 μm and laser current of 160 mA with a exposure time of 10 ms.

3. Results and discussion

3.1. Parametric analysis of continuous high-shear granulation process

3.1.1. Multiple linear regression models for granule and tablet properties

In the present study, multiple linear regression models were developed posterior to the completion of DoE experiments to correlate the properties or responses to the processing conditions or regressors. The raw data of granule and tablet properties were provided in Tables S1 and S2. The selection of optimum terms included in each model necessitated striking a balance between parsimony (fewer independent variables if possible) and accuracy (more independent variables if requisite). Forward stepwise regression commencing with a null model with no predictors but only one intercept was ipso facto deployed to determine a subset of significant model terms, following an automatic process of successively adding or subtracting a regressor until the prespecified stopping rule, e.g., Akaike information criterion with a correction for finite sample sizes (AICc), was minimized. Eventually, the process ensured the goodness of fit for each finalized model without jeopardizing its robustness by overfitting [33].

Based on the stepwise regression, Tables 4 and 5 summarized the *t*-statistic of critical variables in different response surface reduced quadratic models concerning granule and tablet attributes. At the confidence interval of 95 percent, a specific model term with the absolute value of its test statistic greater than the critical value 1.96 was considered to be statistically significant. The larger the *t*-value was, the more influence it can exert on the corresponding response. Certain regressors, for instance the L/S ratio (x_2) and throughput (x_3) for friability in Table 5, were still included in the model despite their small *t*-values, primarily due to the consequential interaction ($x_1 * x_3$) or quadratic (x_2^2) effect induced. Removal of those two main effects would lead to the violation of hierarchical principle that higher order terms in the model also required the inclusion of all its lower order ones.

In addition, the regression statistics (Adj R-Sq and Pred R-Sq) of most models were indicative of satisfactory performance. It was nevertheless noticeable that the figures of merit for granule sizing metrics, D10 and D90, as well as tablet porosity models were relatively low implying more residual variability remained unexplained in the current experiments. Overall, L/S ratio was deemed to be the most essential factor as it was included in the reduced models for almost all granule and tablet attributes whereas throughput was viewed as the least influential one. In terms of granule properties, the *t*-values indicated that an increase in rotation speed or liquid addition gave rise to enlarged size with more uniform distribution, better sphericity and improved flowability. Such an alteration in granulation condition also generated greatly consolidated particles partaking of smaller porosity and enhanced resistance to breakage.

With respect to tablet attributes, $t_{3\ min}$ and $DE_{10\ min}$ decreased while $t_{90\%}$ increased as the L/S ratio or impeller rotation speed elevated to higher levels, irrespective of the throughput settings. Since the curvature and interaction effects in the friability model were significant, the influence of L/S ratio on tablet friability substantially contingent on the levels of rotation speed. Contour plots (refer to Figs. S1–S3) signified that tablets exhibited the largest amount of weight loss during friability testing when both L/S ratio and rotation speed were fixed at their respective intermediate level. In contrast, one factor demonstrated marginal implication if the other parameter was set to low or high conditions. Disintegration time as revealed by Fig. S4 and the *t*-values in Table 5 was negatively related to the shear intensity when throughput was held constant at low level. Nonetheless it was primarily dic-

Table 4
t-Statistic of independent variables and regression statistics of granule response surface reduced quadratic models.

Regressor	*t*-Statistic of independent variables for granule responses									
	D10	D50	D90	Span	Porosity	Strength	Bulk Density	Tapped Density	Hausner Ratio	Aspect Ratio
x_1		3.00		−4.53	−5.07	9.40	4.65	5.26	−2.82	−3.42
x_2	3.52	5.37	3.86	−4.03	−2.81	8.56	2.84		−7.00	−3.61
x_3								−2.24		
$x_1 * x_2$		0.26		3.02		−2.14	−1.55		3.04	2.84
$x_1 * x_3$										
$x_2 * x_3$										
x_1^2				3.35	3.09	−6.79		−2.35		2.92
x_2^2							−2.20			
x_3^2										
Regression Statistics										
Adj R-Sq	0.42	0.69	0.47	0.77	0.71	0.93	0.67	0.69	0.80	0.70
Pred R-Sq	0.28	0.53	0.34	0.63	0.59	0.88	0.53	0.59	0.68	0.57

Table 5
t-Statistic of independent variables and regression statistics of tablet response surface reduced quadratic models.

Regressor	*t*-Statistic of independent variables for tablet responses						
	$t_{3\ min}$	$t_{90\%}$	$DE_{10\ min}$	Tablet Porosity	Friability	Disintegration Time	Tensile Strength
x_1	−4.51	5.78	−4.98		−1.81	1.39	
x_2	−4.32	4.45	−4.21	−1.76	−0.75	4.54	3.34
x_3					0.42	0.27	−3.80
$x_1 * x_2$		3.37					
$x_1 * x_3$					−5.26	7.04	
$x_2 * x_3$						3.83	−6.87
x_1^2					−2.94	3.78	
x_2^2					−3.60		
x_3^2							
Regression Statistics							
Adj R-Sq	0.70	0.80	0.72	0.12	0.82	0.86	0.81
Pred R-Sq	0.63	0.72	0.66	–	0.66	0.44	0.72

tated by water addition amount at the intermediate level of throughput where disintegration process was prolonged as L/S ratio increased (refer to Fig. S5). Besides, this response turned out to be determined by both parameters when powder feeding rate eventually rose to its high level (refer to Fig. S6). Apropos of tensile strength, it consistently declined in conjunction with L/S ratio, especially when throughout was relatively low (refer to Fig. S7). Additionally, all acceptance values were less than 2, indicating excellent tablet content uniformity (not shown). Given that only granules from 250 to 710 μm were selected for tableting, the small AVs also implied limited degree of drug segregation across different granule size fractions.

3.1.2. Overview of the interrelation between observations, CPPs and CQAs

Fig. 2 PLS biplot with the superimposition of pc(corr) and t(corr) for the first and second PLS component. pc(corr) was the vector combining **X** loadings p and **Y** loading weights c scaled as correlation coefficients between **X** and scores t, and **Y** and scores u, respectively. t(corr) was the score vectors re-scaled to the −1 and +1 numerical range based on the ratio of sum of squares of loadings to sum of squares of scores t.

By constructing a PLS2 model, cross-validation suggested two PLS components in modeling the responses with 66.7% and 52.3% variation explained in the **X** and **Y** dataset, respectively. In Fig. 2, PLS biplot as a graphical representation of the PLS regression coefficients of data matrix enabled the simultaneous display and interpretation of the relationship structures among all the DoE runs (observations, row entities), operation conditions (input variables, column entities) and granule and tablet properties (output variables, column entities) in a single context.

The predictor variables with substantial impact were situated distantly from the origin, signifying a tight connection with response variables. To better interpret this plot, a base line can be drawn through the origin and one certain response. With all X-variables and other responses projected orthogonally onto this line, entities located in an opposite direction were negatively correlated whilst those were positively linked if adjacent to each other. Furthermore, the biplot also revealed the parallels and dissimilarities between observations, and facilitated the apprehension of their overall relationships with variables. Observations near the plot origin had average properties.

As illustrated in Fig. 2, L/S ratio and rotation speed possessed higher leverage and were of utmost importance in modulating the CQAs; conversely, the contribution of throughput was poorly described by the model components and thus was not so prominent as the other two parameters. However, given the fact that Lödige CM5 can accommodate the materials feeding rate up to 80 kg/h and that levels of throughput (10–20 kg/h) evaluated in the current study approximated the lowest threshold (10 kg/h), its impact could be of a greater magnitude if granulator fill degree increased.

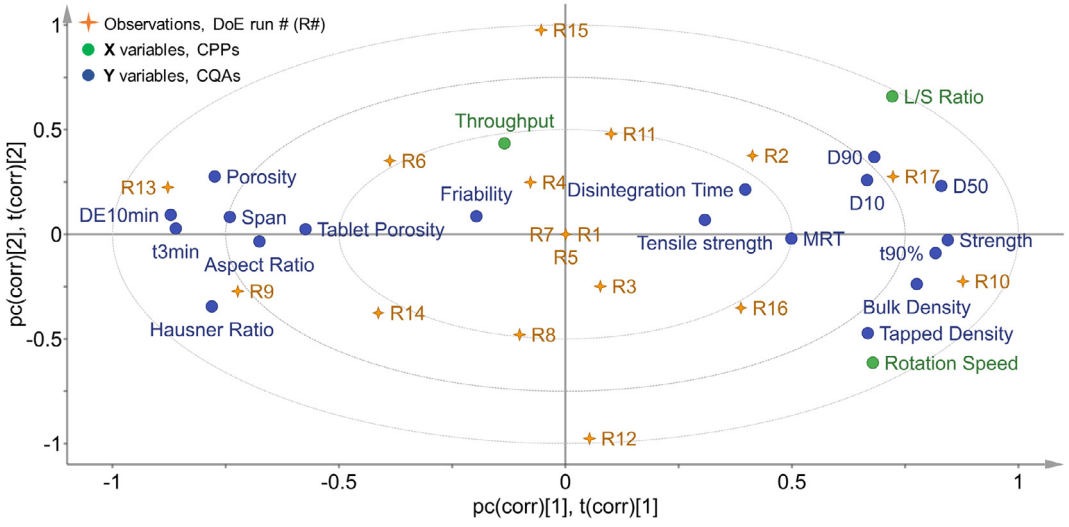

Fig. 2. PLS biplot with the superimposition of pc(corr) and t(corr) for the first and second PLS component. pc(corr) was the vector combining **X** loadings p and **Y** loading weights c scaled as correlation coefficients between **X** and scores t, and **Y** and scores u, respectively. t(corr) was the score vectors re-scaled to the −1 and +1 numerical range based on the ratio of sum of squares of loadings to sum of squares of scores t.

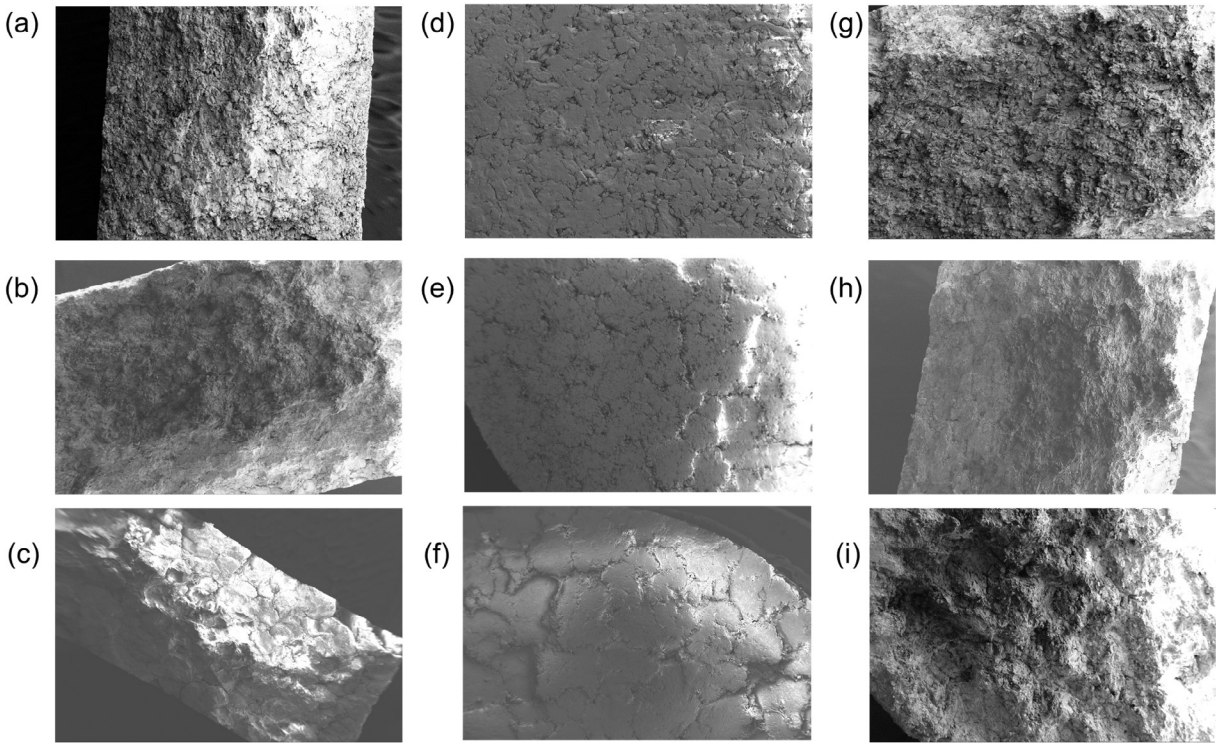

Fig. 3. SEM images of tablets. Run #13: (a), (d) and (g); Run #7: (b), (e) and (h); Run #10: (c), (f) and (i). Cross section of tablets with compression force at 10 kN: (a), (b) and (c); Cross section of tablets with compression force at 24 kN: (g), (h) and (i); Surface of tablets with compression force at 10 kN: (d), (e) and (f).

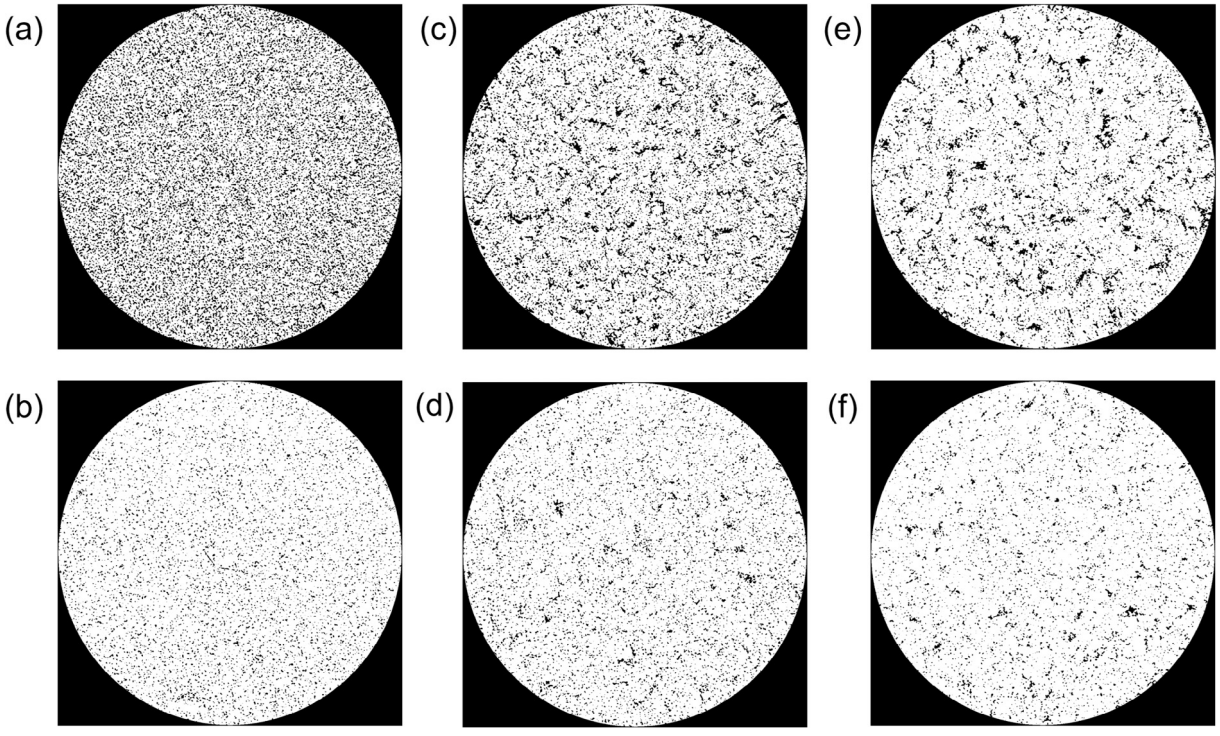

Fig. 4. Tablet physical microstructure within region of interest by 2D binary micro-CT images. Run #13: (a) and (b); Run #7: (c) and (d); Run #10: (e) and (f). Tablets with compression force at 10 kN: (a), (c) and (e); Tablets with compression force at 24 kN: (b), (d) and (f). Groups of white and black pixels represented the solids (object) and pores (background), respectively.

By examining the first latent variable capturing 33.3% and 47.8% variation in **X** and **Y** design matrices respectively, impeller speed and liquid addition amount created a synergistic effect on the characteristics of granules and tablets. Increasing rotation speed promoted granule coalescence primarily stemming from incessant interparticle interactions and intimate liquid-powder mixing at

Table 6
Pore volume information within the volume of interest extracted on the basis of 3D analysis.

Run #	Compression force (kN)	Volume percentage		
		Open pore	Closed pore	Total
13	10	18.40	0.601	18.90
	24	0.767	4.66	5.39
7	10	12.50	2.18	14.40
	24	1.88	4.94	6.72
10	10	7.53	2.58	9.92
	24	0.91	3.97	4.84

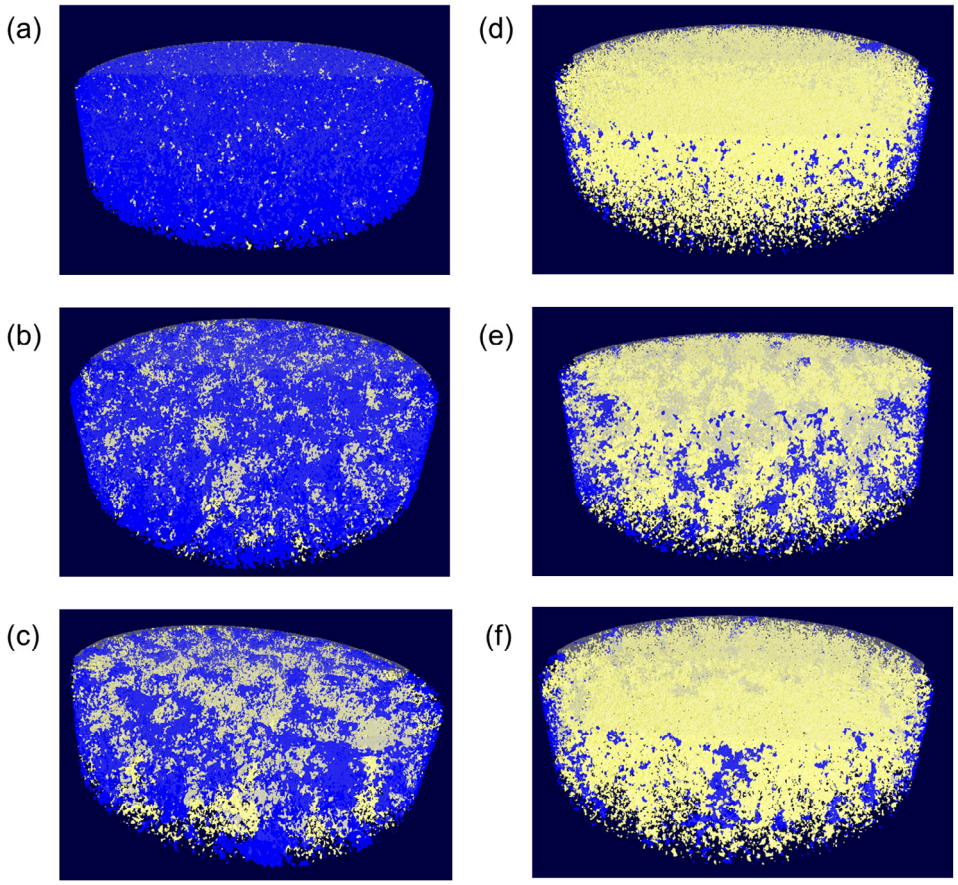

Fig. 5. 3D visualization of tablet open and closed pore networks within the volume of interest. Run #13: (a) and (d); Run #7: (b) and (e); Run #10: (c) and (f). Tablets with compression force at 10 kN: (a), (b) and (c); Tablets with compression force at 24 kN: (d), (e) and (f). Distribution was color-coded to differentiate the open pores (blue) from closed pores (yellow). (For interpretation of the references to colour in this figure legend, the reader is referred to the web version of this article.)

higher agitation intensity. Intensive shear force consolidated particles causing an increase of maximum pore saturation where more free liquid was squeezed into the particle interfacial zones after sufficient deformation and available for further granule growth. L/S ratio governed the granule degree of liquid saturation, which is crucial to the formulation of nuclei, reduction of induction period as well as the subsequent steady growth thereof. Increasing the content of low viscosity binder (water) also eased interparticle friction, rendering the granules more susceptible to densification of smaller voidage owing to the abated dynamic yield strength and bolstered deformability.

With respect to tablet performance, $t_{90\%}$ was positively correlated to the granule strength and negatively correlated to the granule porosity. When granules were more porous, they demonstrated lower strength accompanied by faster disintegration and smaller tensile strength once compacted into tablets. The drug dissolution rate was accordingly more rapid, namely that less time was necessitated achieving 90% of released drug. Analogously, $t_{3\ min}$ and $DE_{10\ min}$ were located near granule porosity and, ipso facto, more APAP was release within the first 3 min, reflecting higher dissolution efficiency in the first 10 min. As regards the observations in Fig. 2, experimental run #13 (R13) and run #10 (R10) epitomized the two extremes of the first PLS component, viz. that R10 produced granules spotlighting the following attributes: larger particle size with more homogeneous distribution, smaller porosity, better flowability, enhanced sphericity, longer residence time, stronger tablet tensile strength, reduced disintegration rate and slower drug release kinetics, while R13 generated granules with the converse properties. Overall, the first factor can be ascribed to the mechanical shear input, with a higher level of which it

simultaneously boosted the growth of nuclei, liquid redistribution and particle consolidaiton.

By examining the second latent variable explaining 33.3% and 4.53% variation in **X** and **Y** design matrices respectively, impeller speed and liquid addition amount showed an antagonistic effect principally on several granule properties. Increasing L/S ratio promoted particle coalescence with larger size metrics yet did not aid in the granule densification while escalating rotation speed caused more breakage and attrition. Experimental run #15 (R15) and run #12 (R12) exemplified the two extremes of the second PLS component with the former producing large porous granules and the latter generating small consolidated granules. It was inferred that the second factor was attributed to the change of torque values in that R15 was operated with the highest L/S ratio and throughput but the lowest rotation speed as opposed to R12 of the lowest L/S ratio and throughput but the highest rotation speed. Granulation mechanism in this scenario was dominated by drop controlled nucleation followed by breakage rather than mechanical dispersion.

3.2. Influence of tablet internal structure on dissolution performance

3.2.1. Morphology and physical microstructure

Tablet dissolution rate is inextricably interwoven with its physical microstructure [20,27]. To understand the process-structure and structure-property relationships, three representative batches of granules (run #7, #10 and #13) were selected and compressed into tablets. Due to distinct processing conditions in Table 3, particles underwent different degrees of deformation and consolidation during granulation. Run #13 produced the most porous granules with a large porosity of 61.9% while run #10 manufactured the most desified granules with a small porosity of 33.7%. One of the DoE center points, run #7, generated granules with an intermediate level of porosity, 46.5%. As shown in Fig. 3, tablets compacted from different granules revealed appreciable discrepancies in their morphology. In terms of run #13, both tablet cross-sectional area and surface were relatively amorphous since the weaker granules were fragmented during the compaction process. In contrast, densified granules from run #10 were more resistant to the compression force and were merely subjected to limited rearrangement and plastic deformation rather than fracture. Therefore, distinct boundaries among contiguous granules on both surface and cross section could be easily discovered. Besides, the morphology of tablets from run #7 was deemed to be between run #10 and run #13, namely that granules experienced partial fragmentation during tableting. However, it seems that all granules were inevitably turned into crumbles when the compression force was improved from 10 kN to 24 kN, despite that tablets in run #13 still demonstrated the most homogeneous appearance.

Fig. 4 reflected the tablets internal structure with one slice of their 2D binary micro-CT images. The region of interest (ROI) referred to the selected region on a single crosssection image. It was apparent that tablets produced with denser granules or higher compression force possessed lower pore volume (less black pixels). The extracted information concerning open and closed pores in volume of interest (VOI) were listed in Table 6 and illustrated in Fig. 5. In comparison to ROI, the VOI referred to the integration of all ROIs across the selected image levels. In 3D space, closed pores were defined as a connected assemblage of black voxels thoroughly surrounded by solid (white) voxels whereas open pores were those space situated within or between solid objects but had connections in 3D to the space outside the objects. It could be seen that with the compression force of 10 kN, an overwhelming majority of the pores in run #13 were

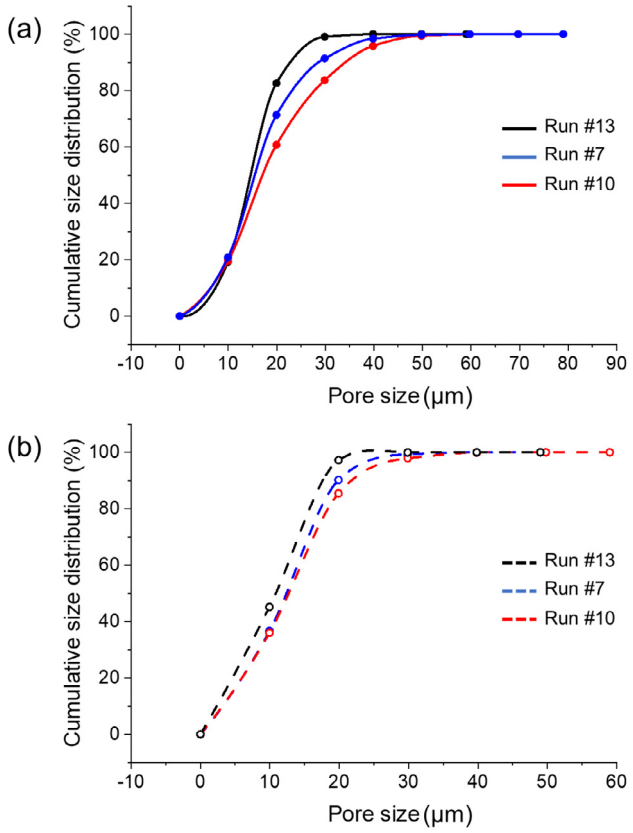

Fig. 6. Cumulative pore size distribution of tablets compressed at (a) 10 kN and (b) 24 kN.

connected to the outside space (blue color in Fig. 5) while more closed pores (yellow color in Fig. 5) were detected for run #10. Also, the overall tablet porosity consistently decreased from run #10 to run # 7 and eventually to run #13. It was inferred that denser granules experienced less deformation and more vigorous inter-particle interactions during compilation, thereby leading to highly consolidated tablets with larger proportion of closed pores. In terms of 24 kN, nevertheless, the tablet porosity for all three batches declined considerably and almost all pores were encircled by the particles. In particular, the cylindrical tablets were surrounded circumferentially by the open pores leaving the closed pores in the inner areas.

The pore size distribution was plotted in Fig. 6 and visualized in 3D in Fig. 7. It could be discovered that the granule porosity was not only synonymous with the overall tablet porosity including the open/closed pore ratio but engendered different tablet pore size distributions. As aptly evinced in Table 6 and Fig. 6(a), although run #10 had smaller overall pore volume compared with run #13, it demonstrated larger pore size in that the stronger granules underwent limited extent of rearrangements during compaction. Again the difference in size distribution became less pronounced as the compression force increased to 24 kN (see Fig. 6(b)), which further corroborated the previous findings that high enough compression force could predominate the tablet morphology and internal structure over granule porosity. Furthermore, Fig. 7 showed that significant amount of pores for run #10_10 kN tablet were colored by red, indicating their size was larger than 10,000 voxels. Instead run #13_10 kN tablet exhibited more pores less than 1000 voxels highlighted by the color of purple. At 24 kN, pores of the latter larger than 10,000 voxels nearly vanished due to

its facile rearrangement and high compressibility while for the former and run #7 the pores in such a size fraction were still detectable.

3.2.2. Real-time monitoring of disintegration and drug release mechanisms

Figs. 8 and 9 depicted the real-time monitoring of disintegration processes of tablets manufactured at 10 and 24 kN, respectively. Specifically, in Fig. 8, due to the presence of massive open pores, water rapidly penetrated into the matrix along with the wetting front consistently moving inward until the whole tablet was eventually soaked with dissolution medium, which gave rise to a fast disintegration and erosion process of the tablets from run #13 and run #7. The corollary of that was fast drug release kinetics following the disruption of structure in light of the hydrophilic property of APAP. In contrast, tablet of run #10 remained relatively integral throughout the entire dissolution process by virtue of the closed pores and stronger interparticle bonding after compaction. Therefore, water penetration into the tablet and the ensuing dissolution of drug were relatively slow. In addition, as evinced in Fig. 9, all tablets exhibited extended disintegration and dissolution behaviors once the compression force enhanced to 24 kN. However, it can be seen that the lamination occurred for all tablets implying the potential of over compression during manufacturing process where excessive force was applied to further induce elastic recovery of particles after their non-reversible fragmentation upon the removal of stress. Hence the contact points or bonding established between adjacent particles were undermined especially when the extent of elastic recovery is amply large.

The drug release parameters in Table 7 and profiles in Fig. 10 were in accordance with their respective disintegration and erosion speed. Particularly, it showed similar dissolution rates in terms of the 24 kN tablets from run #7 and #10, counteracting the implication of granule internal structure and leaving the process less sensitive to tablet porosity variaiton. On the other hand, however, dissolution rate of the tablets at 10 kN reflected a progressive acceleration as granules became more porous from run #10 to run #13, authenticating that engineering granule microstructure was still indispensable for controlling the drug diffusion.

In addition, the particle size distribution after complete tablet disintegration in Fig. 11 further substantiated the aforementationed results. Since original granule size selected for tableting (250–710 μm) was identical for all three batches, the size variation after disintegration embodied the extent of particle resistance to mechanical compression force with porous granules (run #13) inclined to be crushed and densified granules (run #10) in all likelihood being plastically deformed. It was apparent that particle size steadily increased from run #13 to #7 and to #10, confirming the conclusions elicited from Fig. 3. Besides, it was noticeable that size distributions of 24 kN disintegrated tablets shifted to the positive direction of *x*-axis as opposed to those from 10 kN, principally because particles experiencing higher compaction force were still partially combined together even after the tablet disintegration, leading to larger residual aggregates.

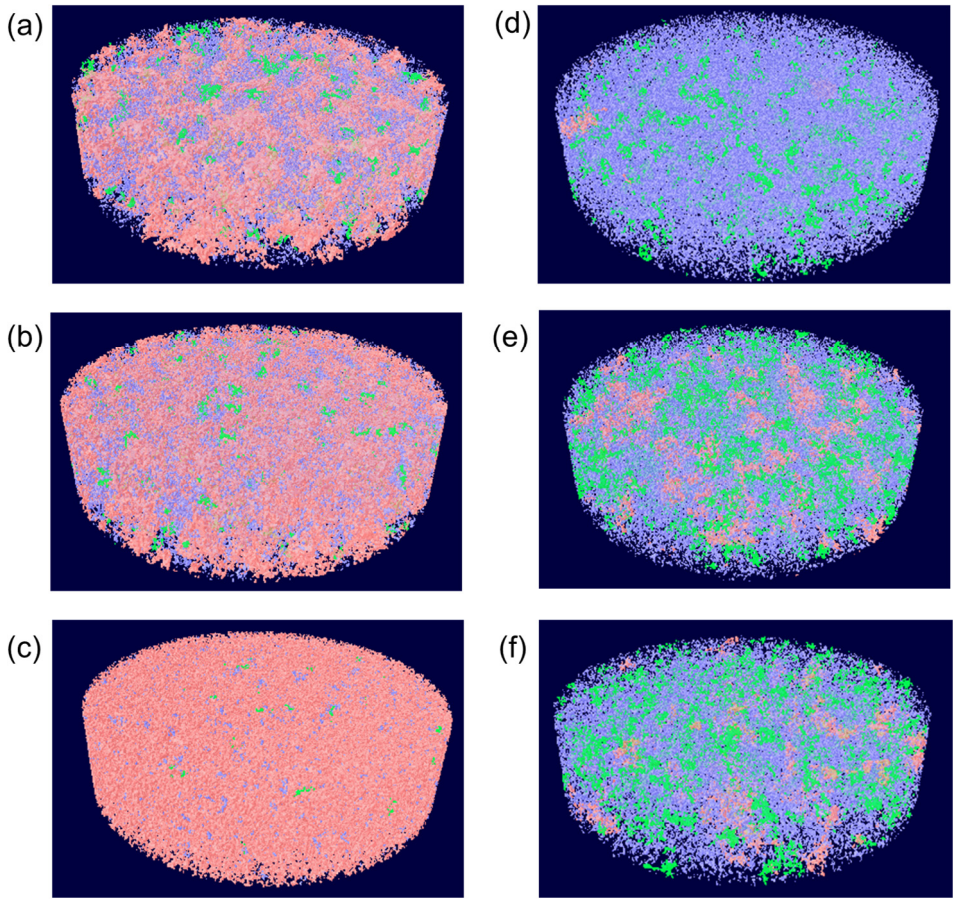

Fig. 7. 3D visualization of tablet pore size distribution within the volume of interest. Run #13: (a) and (d); Run #7: (b) and (e); Run #10: (c) and (f). Tablets with compression force at 10 kN: (a), (b) and (c); Tablets with compression force at 24 kN: (d), (e) and (f). The color code represented the pore volume within different size fractions: larger than 10,000 voxels (red), between 1000 and 10,000 voxels (green) and smaller than 1000 voxels (purple). (For interpretation of the references to color in this figure legend, the reader is referred to the web version of this article.)

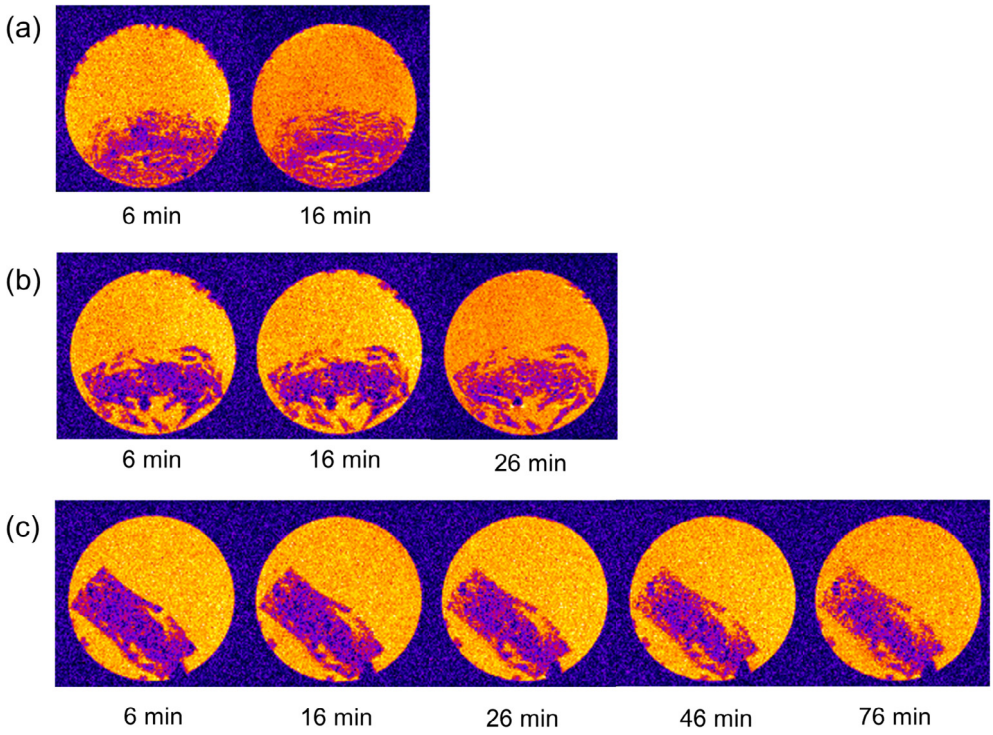

Fig. 8. *In situ* real-time observation of disintegration of tablets compressed at 10 kN by MRI. (a) Run #13, (b) Run # 7 and (c) Run # 10. The individual snapshots corresponded to different representative time points of respective MRI movies during dissolution. Colors within the field of view denoted dissolution medium (orange) and tablet (purple). (For interpretation of the references to color in this figure legend, the reader is referred to the web version of this article.)

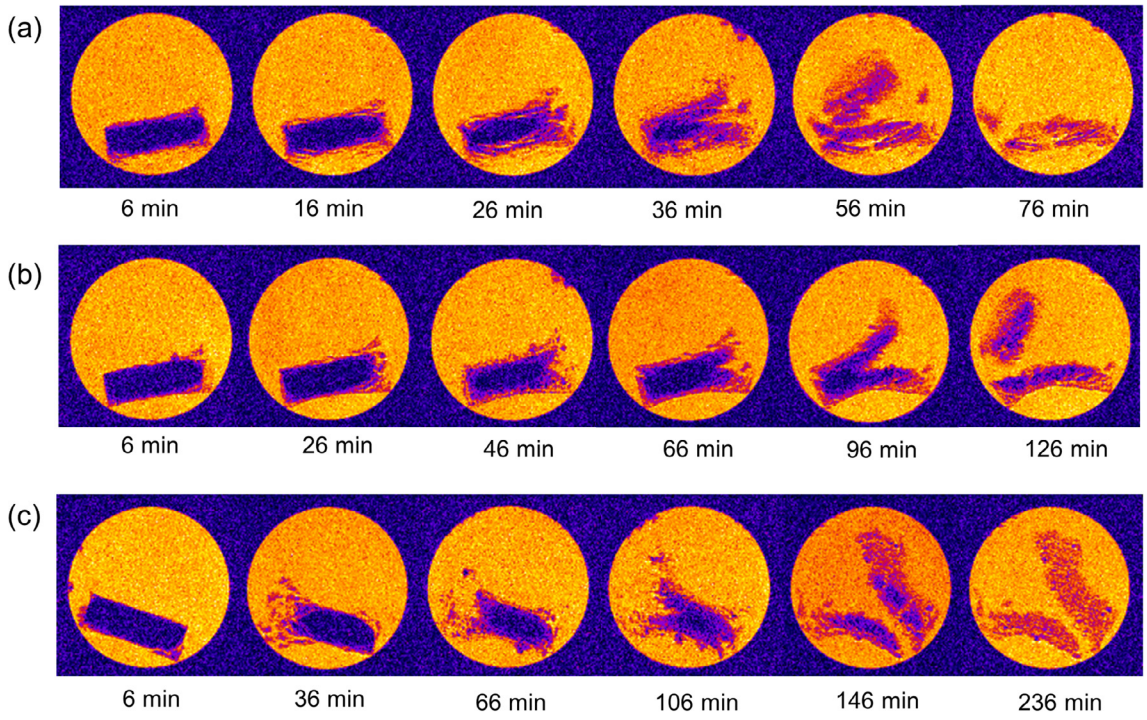

Fig. 9. *In situ* real-time observation of disintegration of tablets compressed at 24 kN by MRI. (a) Run #13, (b) Run # 7 and (c) Run # 10. The individual snapshots corresponded to different representative time points of respective MRI movies during dissolution. Colors within the field of view denoted dissolution medium (orange) and tablet (purple). (For interpretation of the references to color in this figure legend, the reader is referred to the web version of this article.)

3.3. Influence of drug agglomerate size distribution on dissolution performance

3.3.1. Tablet chemical microstructure

Aside from physical microstructure, tablet 3D chemical microstructure was also unveiled by the Raman imaging. Fig. 12 (a) showed the distribution of all ingredients in a tablet produced from continuously mixed (CM) blends while (b) conveyed analogous information in a tablet with raw materials premix prepared by batch mixing (BM). Although granulation settings were identical for both scenarios (run #13), stark difference in drug agglomerate size distribution was discovered. Notably continuous

Table 7
Drug release parameters of tablets produced at different premixing, granulation, and compression conditions.

Run#	Premixing method	Compression force (kN)	$t_{3\ min}$ (%)	$t_{90\%}$ (min)	$DE_{10\ min}$ (%)	$DE_{90\ min}$ (%)
13	Continuous	10	80.97	5.00	77.18	87.43
	Continuous	24	12.50	45.51	20.08	70.71
	Batch	10	71.15	5.63	73.52	87.09
7	Continuous	10	51.67	8.52	62.89	85.87
	Continuous	24	7.50	110.12	10.82	51.86
	Batch	10	25.43	19.11	41.76	81.55
10	Continuous	10	26.11	21.25	39.76	80.87
	Continuous	24	6.62	98.83	11.33	52.69
	Batch	10	12.66	44.09	25.87	72.78

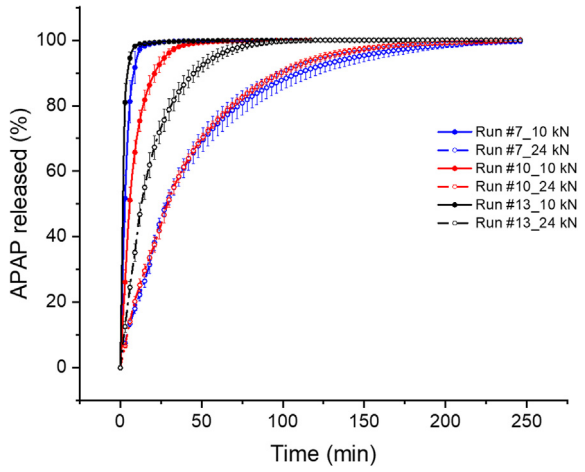

Fig. 10. Drug release kinetics of tablets produced at different granulation conditions and compression forces.

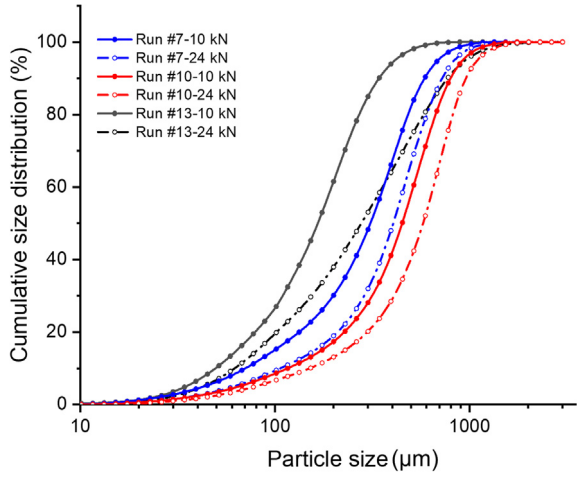

Fig. 11. Cumulative particle size distribution after tablet complete disintegration in the dissolution medium.

convective mixing coupled with delumping by conical mill were able to deliver more efficient micro- (dispersive) and macro- (distributive) mixing where both cohesive drug and excipients were uniformly dispersed and distributed. Specifically, the high-shear mixing associated with conical mill provided intense planar-shear effects for de-agglomeration. The convective mixing accompanied by a relatively low-shear level contributed to stretching the interfacial area between ingredients absent from cohesive resistance and distributing them homogeneous throughout the product volume. In contrast, large drug agglomerates remained in the tablet when all constituents were premixed in the gravity-driven low-shear batch tote blender. Similarly, outcome of Figs. 13 and 14 under the respective granulation condition of run #7 and #10 further ascertained the aforementioned inference, i.e, superior blend uniformity and structure at the output of continuous mixer with small scale of segregation and low intensity of segregation.

Furthermore, Figs. 15–17 specifically focused on APAP rather than all ingredients in the tablets and provided a more straightforward illustration of the drug agglomerate size distribution. For instance, in Fig. 15(a) and (c), color code identified the APAP spatial distribution in tablets from continuous and batch mixing blends by adopting the first classification of particle/agglomerate size fractions. Green stood for the size smaller than 50 μm; red represented the range from 50 to 250 μm; blue highlighted the particles larger than 250 μm. Fig. 15(b) and (d) provided similar information but utilized the second classification of size fractions that the upper size threshold for visualizing APAP agglomerates increased from 250 to 400 μm. By comparing Fig. 15(a)–(c), more blue domains can be observed in the latter, evidencing more large clumps of drug agglomerates in the BM tablet. Moreover, once the upper size threshold value increased from 250 to 400 μm, all blue domains in CM tablet turned into red (see yellow dash circles in Fig. 15(a) and (b)), indicating the non-existence of agglomerate larger than 400 μm. Nonetheless for BM tablet several APAP domains still remained as blue, i.e., larger than 400 μm, albeit the increase of upper size threshold (see Fig. 15(c) and (d)). The same conclusions can be elicited by examining Figs. 16 and 17, irrespective of the granulation parameters. Also, cumulative size distribution in Fig. 18 was consistent with the previous findings that the curves of all BM tablets shifted to the positive direction of *x*-axis implying their relatively large size distribution. Therefore, despite that wet granulation accommodated material variability better than direct compression, heterogeneity of chemical structure within tablets was still discovered. Additionally, the degree of heterogenetiy was contingent on whether the dry powders were pre-blended in a batch blender or a continuous blender.

3.3.2. Dissolution performance

The dissolution profiles in Fig. 19 and parameters in Table 7 demonstrated remarkable difference regarding the dissolution behavior between CM and BM tablets. According to the student's *t*-test (not shown), drug agglomerate size had a statistically significant impact on the release kinetics. With the identical granulation, tableting and dissolution conditions, tablet physical microstructure in all likelihood were similar to each other. The variation in APAP dissolution rate was thus believed to be stemming from the raw materials pre-mixing stage, viz. the discrepancy in drug

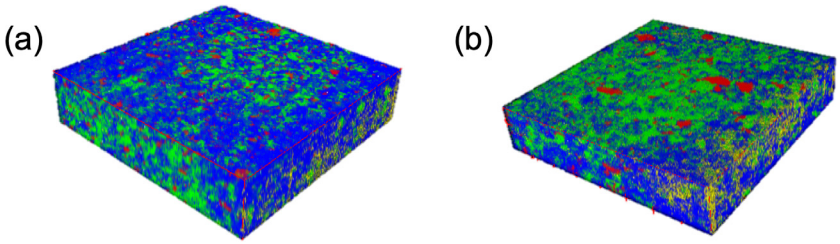

Fig. 12. 3D visualization of tablet ingredients distribution. APAP, MCC, Lactose and PVP were color-coded by red, blue, green and yellow, respectively. (a) Multi-component distribution of CM run #13. (b) Multi-component distribution of BM run #13. (For interpretation of the references to color in this figure legend, the reader is referred to the web version of this article.)

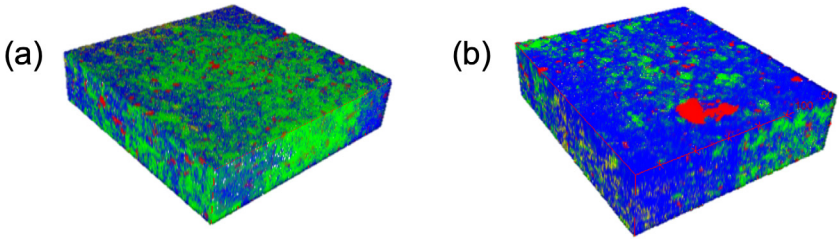

Fig. 13. 3D visualization of tablet ingredients distribution. APAP, MCC, Lactose and PVP were color-coded by red, blue, green and yellow, respectively. (a) Multi-component distribution of CM run #7. (b) Multi-component distribution of BM run #7. (For interpretation of the references to color in this figure legend, the reader is referred to the web version of this article.)

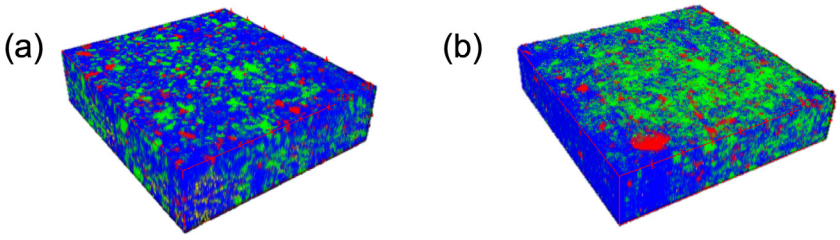

Fig. 14. 3D visualization of tablet ingredients distribution. APAP, MCC, Lactose and PVP were color-coded by red, blue, green and yellow, respectively. (a) Multi-component distribution of CM run #10. (b) Multi-component distribution of BM run #10. (For interpretation of the references to color in this figure legend, the reader is referred to the web version of this article.)

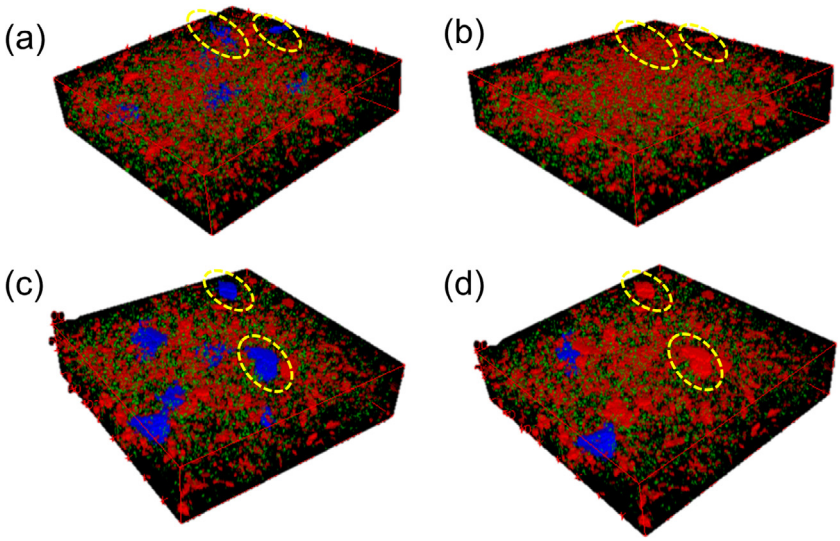

Fig. 15. 3D visualization of tablet drug agglomerate size distribution. The color code indicated the agglomerate volume in different size fractions. For (a) CM run #13 and (c) BM run #13, blue, red and green represented the size larger than 250 μm, between 250 and 50 μm, less than 50 μm, respectively. For (b) CM run #13 and (d) BM run #13, blue, red and green represented the size larger than 400 μm, between 400 and 50 μm, less than 50 μm, respectively. (For interpretation of the references to color in this figure legend, the reader is referred to the web version of this article.)

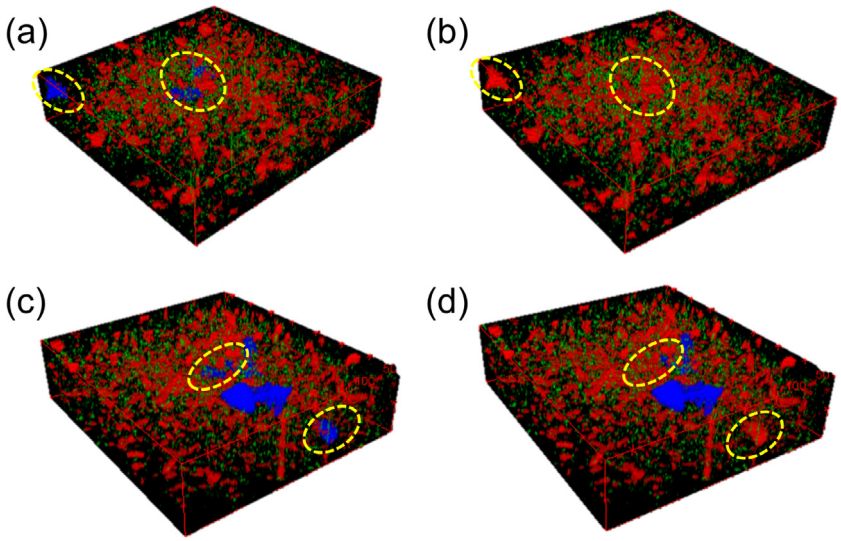

Fig. 16. 3D visualization of tablet drug agglomerate size distribution. The color code indicated the agglomerate volume in different size fractions. For (a) CM run #7 and (c) BM run #7, blue, red and green represented the size larger than 250 μm, between 250 and 50 μm, less than 50 μm, respectively. For (b) CM run #7 and (d) BM run #7, blue, red and green represented the size larger than 400 μm, between 400 and 50 μm, less than 50 μm, respectively. (For interpretation of the references to color in this figure legend, the reader is referred to the web version of this article.)

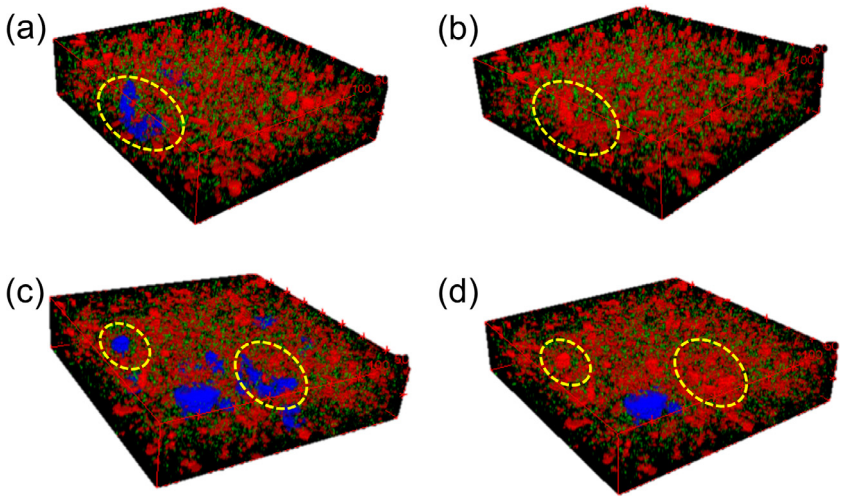

Fig. 17. 3D visualization of tablet drug agglomerate size distribution. The color code indicated the agglomerate volume in different size fractions. For (a) CM run #10 and (c) BM run #10, blue, red and green represented the size larger than 250 μm, between 250 and 50 μm, less than 50 μm, respectively. For (b) CM run #10 and (d) BM run #10, blue, red and green represented the size larger than 400 μm, between 400 and 50 μm, less than 50 μm, respectively. (For interpretation of the references to color in this figure legend, the reader is referred to the web version of this article.)

agglomerate size. It can be seen that all BM tablets displayed slackened release rate as opposed to their CM counterparts. In the present study, the grade of APAP used was semi-fine with a median diameter of 29.8 μm. As a result, powder exhibited less desirable flowability and primary particles had a high tendency to form aggregates during mixing where cohesion and adhesion forces composed of intermolecular forces (van der Waals interactions and hydrogen bonding), electrostatic interactions (contact potential) and capillary forces (liquid bridge between particles and solid bridging due to crystal bonding) had played a vital role [22]. In the following dissolution process, agglomerates with large size or high packing fractions minimized the drug surface exposed to the surrounding medium and was unable to be readily dispersed, thereby resulting in delayed drug release kinetics. By switching to the continuous mixing, breakage of cohesive intra-agglomerate bonds and the concomitant highly dispersed particles could effectively enhance the drug exposure surface area as well as the ensuing dissolution rate.

Moreover, the interdependence of physical and chemical microstructures can be unravelled by scrutinizing the dissolution profiles in Fig. 19. Although the powder dispersion in Comil expedited the release of active ingredient for all CM tablets, in essence such a gap was perpetually narrowed in comparison to the BM tablets as granule or tablet porosity increased. The difference caused by the two premixing methods for experiment run #13 was nearly indiscernible. Consequently, a consolidated physical microstructure was capable of amplifying the effect of drug agglomerate size by delaying the infiltration process of dissolution medium, which made the dissolution of close-packed drug aggregates even more slower. For the BCS class I drug APAP, a highly porous structure ensured the immediate tablet decomposition thereby minimizing the influence of interparticle cohesiveness.

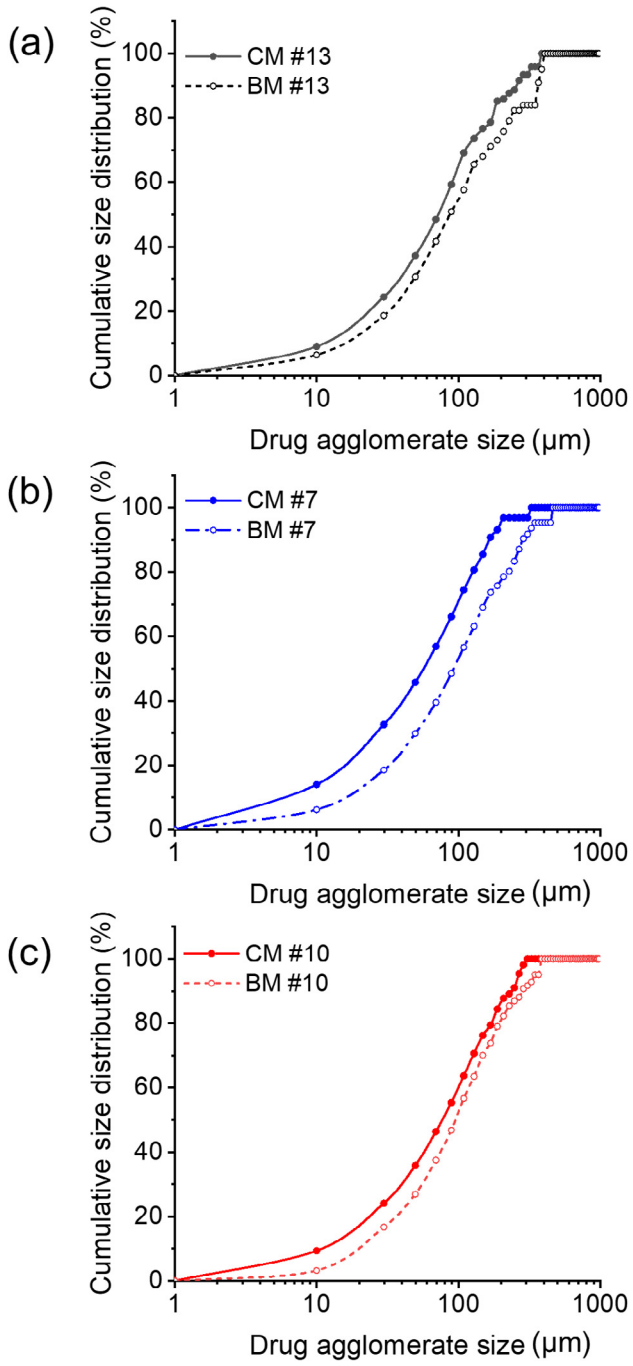

Fig. 18. Cumulative drug agglomerate size distribution of tablets produced with distinct raw material premixing methods. (a) Run #13, (b) Run #7, (c) Run #10.

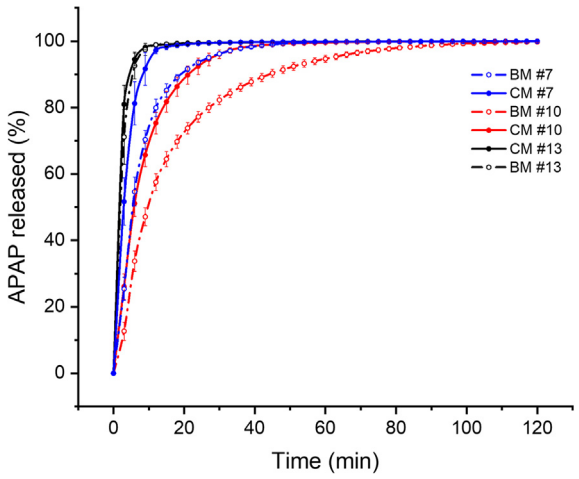

Fig. 19. Drug release kinetics of tablets produced with different raw material premixing methods and granulation conditions.

4. Conclusions

In this study, DoE and multivariate data analysis were used to comprehensively investigate the continuous high-shear granulation process. L/S ratio and impeller rotation speed showed predominant effect over powder feeding rate on the underlying granulation rate processes that further determined the critical attributes of granules and tablets. L/S ratio mainly controlled the particle degree of liquid saturation while rotation speed was a key factor of adjusting the mechanical shear input. The process parameters were capable of modulating tablet performance via altering granule properties, primarily size distribution and porosity.

Besides, the present work demonstrated the essence of in-depth understanding of microstructure that enabled the effective trouble shooting and diagnosis of performance deficiencies in drug product design. Several complementary imaging techniques were implemented to uncover the interrelationship among operation conditions, heterogeneous structure and dosage form property in continuous tablet manufacturing. Dissolution mechanisms with different granulation conditions were expounded by correlating the tablet physical microstructure to disintegration speed. It was found that higher compression force and denser granules resulted in smaller tablet porosity with more closed pores, which subsequently delayed the matrix erosion and impeded the drug release. Moreover, the influence of drug agglomerate size on tablet dissolution was also demonstrated by leveraging two distinct raw materials premixing methods. In contrast to low-shear batch mixing, continuous mixing enabled better deagglomeration effect, thus facilitating the release process on account of more dispersed small drug aggregates. Therefore, a rationally defined and strictly tailored microstructure is in compliance with the QbD principles to guarantee consistent product quality, which is in turn determined by a judicious selection of materials and manufacturing routes.

Acknowledgement

The authors would like to thank Rutgers University Engineering Research Center for Structured Organic Particulate Systems for funding this work. We also gratefully acknowledge Scott Tandy from H2Optx, Inc for experimental suggestions and instrument training.

Appendix A. Supplementary material

Supplementary data to this article can be found online at https://doi.org/10.1016/j.apt.2019.04.028.

References

[1] S.D. Schaber, D.I. Gerogiorgis, R. Ramachandran, J.M.B. Evans, P.I. Barton, B.L. Trout, Economic analysis of integrated continuous and batch pharmaceutical manufacturing: a case study, Ind. Eng. Chem. Res. 50 (2011) 10083–10092.
[2] W. Meng, K.S. Rao, R.D. Snee, R. Ramachandran, F.J. Muzzio, A comprehensive analysis and optimization of continuous twin-screw granulation processes via sequential experimentation strategy, Int. J. Pharmaceut. 556 (2019) 349–362.
[3] M. Fonteyne, J. Vercruysse, F. De Leersnyder, B. Van Snick, C. Vervaet, J.P. Remon, T. De Beer, Process analytical technology for continuous manufacturing of solid-dosage forms, TrAC Trends Anal. Chem. 67 (2015) 159–166.

[4] S. Lee, T. O'Connor, X. Yang, C. Cruz, S. Chatterjee, R. Madurawe, C.V. Moore, L. Yu, J. Woodcock, Modernizing pharmaceutical manufacturing: from batch to continuous production, J. Pharm. Innov. (2015) 1–9.
[5] S.M. Iveson, J.D. Litster, K. Hapgood, B.J. Ennis, Nucleation, growth and breakage phenomena in agitated wet granulation processes: a review, Powder Technol. 117 (2001) 3–39.
[6] C. Vervaet, J.P. Remon, Continuous granulation in the pharmaceutical industry, Chem. Eng. Sci. 60 (2005) 3949–3957.
[7] L.X. Yu, G. Amidon, M.A. Khan, S.W. Hoag, J. Polli, G.K. Raju, J. Woodcock, Understanding pharmaceutical quality by design, AAPS J. 16 (2014) 771–783.
[8] L.X. Yu, Pharmaceutical quality by design: product and process development, understanding, and control, Pharm. Res. 25 (2008) 781–791.
[9] J. Vercruysse, D.C. Diaz, E. Peeters, M. Fonteyne, U. Delaet, I. Van Assche, T. De Beer, J.P. Remon, C. Veryaet, Continuous twin screw granulation: influence of process variables on granule and tablet quality, Eur. J. Pharm. Biopharm. 82 (2012) 205–211.
[10] J. Vercruysse, M. Toiviainen, M. Fonteyne, N. Helkimo, J. Ketolainen, M. Juuti, U. Delaet, I. Van Assche, J.P. Remon, C. Vervaet, T. De Beer, Visualization and understanding of the granulation liquid mixing and distribution during continuous twin screw granulation using NIR chemical imaging, Eur. J. Pharm. Biopharm. 86 (2014) 383–392.
[11] M.F. Saleh, R.M. Dhenge, J.J. Cartwright, M.J. Hounslow, A.D. Salman, Twin screw wet granulation: effect of process and formulation variables on powder caking during production, Int. J. Pharmaceut. 496 (2015) 571–582.
[12] H. Liu, S.C. Galbraith, B. Ricart, C. Stanton, B. Smith-Goettler, L. Verdi, T. O'Connor, S. Lee, S. Yoon, Optimization of critical quality attributes in continuous twin-screw wet granulation via design space validated with pilot scale experimental data, Int. J. Pharmaceut. 525 (2017) 249–263.
[13] M.F. Saleh, R.M. Dhenge, J.J. Cartwright, M.J. Hounslow, A.D. Salman, Twin screw wet granulation: Binder delivery, Int. J. Pharmaceut. 487 (2015) 124–134.
[14] N. Willecke, A. Szepes, M. Wunderlich, J.P. Remon, C. Vervaet, T. De Beer, A novel approach to support formulation design on twin screw wet granulation technology: Understanding the impact of overarching excipient properties on drug product quality attributes, Int. J. Pharmaceut. (2018).
[15] A. Kumar, M. Alakarjula, V. Vanhoorne, M. Toiviainen, F. De Leersnyder, J. Vercruysse, M. Juuti, J. Ketolainen, C. Vervaet, J.P. Remon, K.V. Gernaey, T. De Beer, I. Nopens, Linking granulation performance with residence time and granulation liquid distributions in twin-screw granulation: an experimental investigation, Eur. J. Pharm. Sci. 90 (2016) 25–37.
[16] A.S. El Hagrasy, J.D. Litster, Granulation rate processes in the kneading elements of a twin screw granulator, AICHE J. 59 (2013) 4100–4115.
[17] J. Axel Zeitler, T. Rades, Interdependence of dosage form microstructure and performance, Pharm. Res. (2017) 1–3.
[18] W. Meng, L. Kotamarthy, S. Panikar, M. Sen, S. Pradhan, M. Marc, J.D. Litster, F.J. Muzzio, R. Ramachandran, Statistical analysis and comparison of a continuous high shear granulator with a twin screw granulator: effect of process parameters on critical granule attributes and granulation mechanisms, Int. J. Pharmaceut. 513 (2016) 357–375.
[19] S. van den Ban, D.J.J.P.R. Goodwin, The impact of granule density on tabletting and pharmaceutical product, Performance 34 (2017) 1002–1011.
[20] M.A. Ansari, F. Stepanek, The effect of granule microstructure on dissolution rate, Powder Technol. 181 (2008) 104–114.
[21] D. Markl, J. Sauerwein, D.J. Goodwin, S. van den Ban, J.A. Zeitler, Non-destructive determination of disintegration time and dissolution in immediate release tablets by terahertz transmission, Measurements 34 (2017) 1012–1022.
[22] K. Kale, K. Hapgood, P. Stewart, Drug agglomeration and dissolution – What is the influence of powder mixing?, Eur J. Pharm. Biopharm. 72 (2009) 156–164.
[23] M.M. de Villiers, Influence of agglomeration of cohesive particles on the dissolution behaviour of furosemide powder, Int. J. Pharmaceut. 136 (1996) 175–179.
[24] P.J. Stewart, F.-Y. Zhao, Understanding agglomeration of indomethacin during the dissolution of micronised indomethacin mixtures through dissolution and de-agglomeration modeling approaches, Eur. J. Pharm. Biopharm. 59 (2005) 315–323.
[25] F.-Y. Zhao, P.J. Stewart, Modeling the deagglomeration of micronized benzodiazepines from powder mixtures added to dissolution media, J. Pharm. Sci. 93 (2004) 1618–1627.
[26] C.C. Sun, Microstructure of tablet—pharmaceutical significance, assessment, and engineering, Pharm. Res. 34 (2017) 918–928.
[27] B. Crean, A. Parker, D.L. Roux, M. Perkins, S.Y. Luk, S.R. Banks, C.D. Melia, C.J. Roberts, Elucidation of the internal physical and chemical microstructure of pharmaceutical granules using X-ray micro-computed tomography, Raman microscopy and infrared spectroscopy, Eur. J. Pharm. Biopharm. 76 (2010) 498–506.
[28] T. Allen, Powder Sampling and Particle Size Determination, Elsevier, Amsterdam, 2003.
[29] M.J. Adams, M.A. Mullier, J.P.K. Seville, Agglomerate strength measurement using a uniaxial confined compression test, Powder Technol. 78 (1994) 5–13.
[30] J.T. Fell, J.M. Newton, Determination of tablet strength by the diametral-compression test, J. Pharm. Sci.-Us 59 (1970) 688–691.
[31] P. Costa, J.M. Sousa Lobo, Modeling and comparison of dissolution profiles, Eur. J. Pharm. Sci. 13 (2001) 123–133.
[32] K. Punčochová, A.V. Ewing, M. Gajdošová, N. Sarvašová, S.G. Kazarian, J. Beránek, F. Štěpánek, Identifying the mechanisms of drug release from amorphous solid dispersions using MRI and ATR-FTIR spectroscopic imaging, Int. J. Pharmaceut. 483 (2015) 256–267.
[33] R.B. Bendel, A.A. Afifi, Comparison of stopping rules in forward "Stepwise" regression, J. Am. Stat. Assoc. 72 (1977) 46–53.